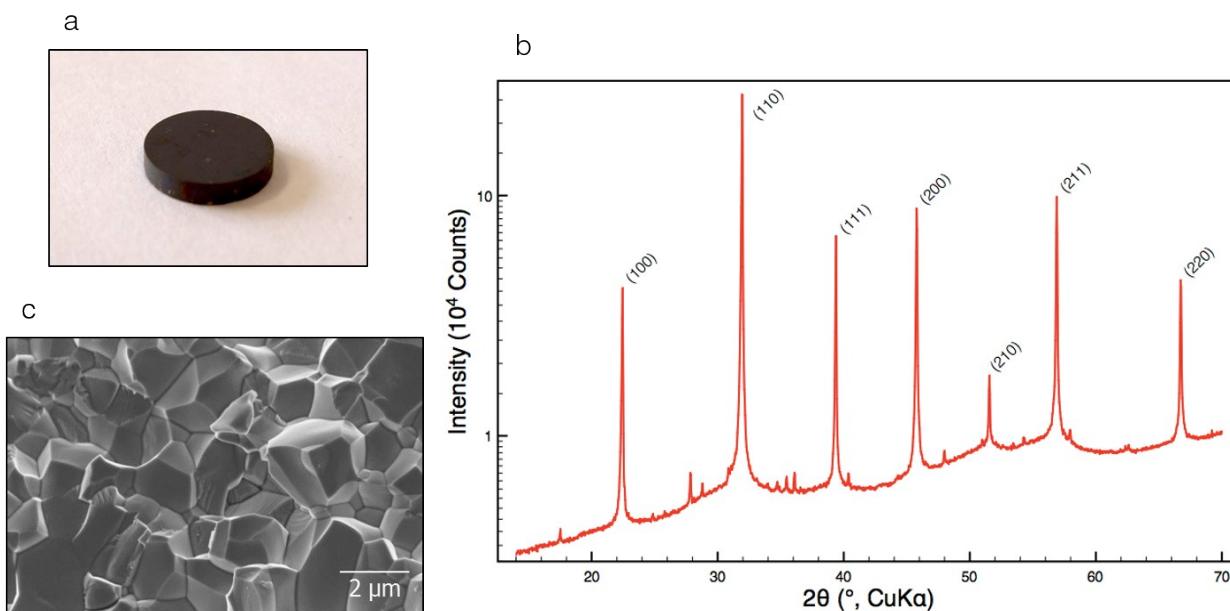


## Supporting Information

### Sample description

The majority of experiments were performed on polycrystalline ceramics with the overall composition  $(\text{BiFe}_{0.9}\text{Co}_{0.1}\text{O}_3)_{0.4}-(\text{Bi}_{1/2}\text{K}_{1/2}\text{TiO}_3)_{0.6}$  (BFC-BKT). Fig. S1 gives basic information on sample appearance, microstructure and crystal structure.



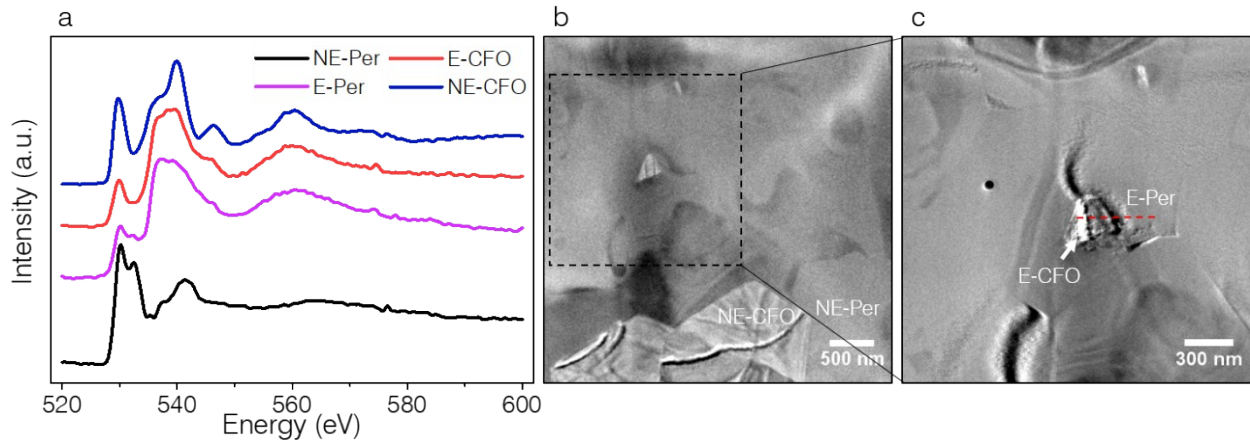
**Figure S1. Structural characterisation of BFC-KBT ceramics.** a) Photo of a typical sintered BFC-BKT ceramic pellet. b) Powder X-ray diffraction pattern recorded at room temperature with  $\text{Cu K}\alpha$  radiation. Diffraction peaks due to  $\text{Cu K}\alpha_2$  radiation were removed. c) SEM images of a fractured ceramic showing the grain structure.

Fig. S1a shows a typical ceramic sintered pellet of BFC-BKT while the SEM image in Fig. S1c shows the grain structure with grain sizes varying between  $0.8 - 4 \mu\text{m}$  and an average grain size of

1.81  $\mu\text{m}$  as determined by linear intercept method. Fig. S1b represents a powder X-ray diffraction pattern taken from a sintered and crushed pellet. The material has a pseudo-cubic perovskite crystal-structure due to absence of characteristic peak splitting for example from (100) and (111) peaks, which is typical for relaxor ferroelectrics.

### Scanning-transmission X-ray microscopy

In an effort to further support the results by PFM, which suggest that CFO cores might be piezoelectric, we carried out X-ray absorption spectroscopy (XAS) at the O *K*-edge. To achieve the necessary lateral resolution for measuring local XAS on the few hundred nanometer sized CFO cores, we utilized scanning-transmission X-ray microscopy (STXM), which has a lateral resolution of approx. 45 nm. We recorded O *K*-edge spectra (with an energy resolution of approx. 1.6 eV), since the hybridizations of O-orbitals with orbitals of metal cations can be sensitive to small structural changes. O *K*-edge spectra show the O2*p*-projected unoccupied density of states and near onset give information, for the present compounds, on the hybridizations of O with the transition metals (TMs).



**Figure S2. Scanning-transmission X-ray microscopy absorption spectroscopy (STXM-XAS).**

**a)** O K-edge spectra of epitaxial CFO (E-CFO), epitaxial perovskite (E-Per), non-epitaxial CFO (NE-CFO) and non-epitaxial perovskite (NE-Per) were measured on a lamella type sample with a thickness of approx. 80 nm. **b, c)** BF-TEM images showing sample regions from which XAS spectra were obtained. The red dashed line in **c** indicates the region on which spectra of E-CFO and E-Per spectra were recorded.

Fig. S2 a shows O K-edge spectra of an epitaxial CFO core (E-CFO) and its perovskite shell (E-Per), which are compared to those of a non-epitaxial large CFO grain (NE-CFO) and perovskite matrix that is not part of a core-shell grain (NE-Per). The sample regions from which spectra were obtained are indicated in Fig. S2 b and c. The spectrum for E-CFO was measured as a line scan across the whole core, and for E-Per in a region close to the core-shell interface (see red dashed line in Fig. S2 c). Similar spectra as for NE-CFO and NE-Per were obtained on other non-epitaxial CFO grains and non-core-shell perovskite grains, respectively.

Due to the multitude of elements, hybridizations, structures and strain, valence and spin states involved in the spectra only a qualitative discussion is possible. First of all, it is striking that the spectra of E-CFO and E-Per differ very significantly from their non-epitaxial counterparts. Furthermore, the spectrum of NE-CFO is in good agreement with spectra of CFO[1] and Fe<sub>3</sub>O<sub>4</sub>[2] reported in literature, while the spectrum of NE-Per is similar to spectra of doped BFO.[3]

For CFO spectra, the lowest energy region from 527-533 eV corresponds to hybridisations of O 2*p* to Co and Fe 3*d* orbitals. This peak is similar to LaCoO<sub>3</sub>[4], [5] or Fe<sub>3</sub>O<sub>4</sub>[2] spectra.

Just a single peak is observed in this energy range, due to the inequivalent TM lattice sites and the relatively small crystal-field splitting. For the perovskite, however, two separate peaks at approx. 530 and 532.5 eV appear in this onset region and are probably due to (O 2*p* hybridizations

with) Ti, Fe  $3d$  states and Bi  $6s$  states, respectively. The next higher energy region from 534 eV and above corresponds most likely to Co, Fe  $4sp$  orbitals for CFO and to Ti, Fe  $4sp$  and Bi  $6p$  orbitals for the BKT/BFO perovskite. For both CFO and the perovskite, the main difference between the “E” and the corresponding “NE” spectrum is an apparent shift of spectral weight over several eV: the peaks at onset and around 530-533 eV are reduced for the epitaxial “E” version while the left shoulder of the “ $4sp$ -peak” at about 537 eV is increased by approximately the same amount. Many different processes may lead to such an apparent shift. Just to name a few: While classical charge-carrier doping alone would only affect the  $3d$  peak at onset a significant transfer of spectral weight upon doping (to the so-called upper Hubbard band, UHB) is known to occur in strongly correlated electron systems.[6], [7] Such systems are frequently found among 3d transition-metal based oxides. An interplay of correlation, charge disproportionation, and lattice effects sometimes leads to the emergence of bipolarons, also concomitant with a transfer of spectral weight away from onset.[8]

The obvious difference between the non-epitaxial and epitaxial phases and the similarities in the spectra of E-CFO and E-Per are very intriguing. Further, systematic investigations would be needed to clearly identify the mechanism(s) underlying this effect. Yet even at this point, and together with the experimental evidence from PFM, this is another indication for strong coupling between the perovskite phase and CFO cores.

### **Mechanism of core-shell formation**

In BFC-BKT ceramics there also exist other CFO grains, which do not exhibit a core-shell structure and thus have no epitaxial relation with the matrix. These non-epitaxial CFO grains are larger than core-grains at least by a factor of five. Furthermore, no ME coupling effects were

observed by scanning probe techniques for those CFO grains. Fig. S3 a shows a PFM image of a large CFO grain, which is clearly not piezoelectric, since it exhibits a homogenous PFM amplitude corresponding to the PFM background signal.

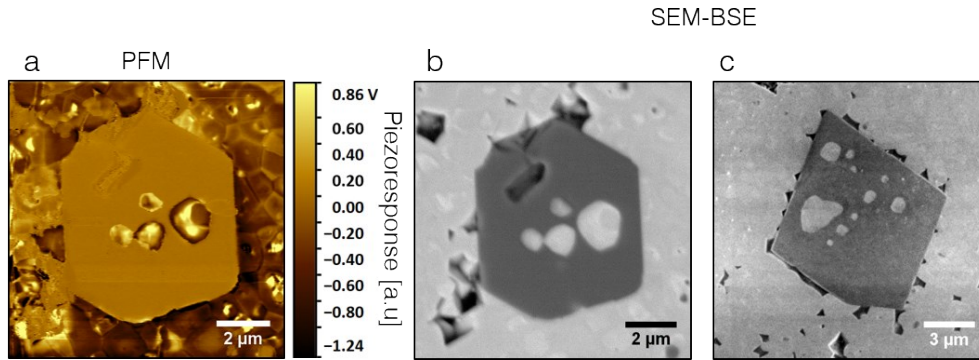


**Figure S3. Non-epitaxial CFO grains in BFC-BKT ceramics.** **a)** VPFM X-Amplitude (mixed signal) of a large CFO grain inside a perovskite matrix. **b)** SEM-BSE image of the same region as in **a)**. The CFO grain is not piezoelectric as visible in PFM. **c)** SEM-BSE image of another CFO grain exhibiting an almost idiomorphous shape of an octahedron, indicating an earlier crystal growth of CFO as compared to the perovskite phase. All of the above CFO grains do not exhibit an epitaxial relation with the perovskite matrix, in contrast to CFO cores shown in Fig. 2 and 3.

In case of these large grains, which do not exhibit a core-shell type structure, we found almost exclusively CFO and very few  $\alpha$ -Fe<sub>2</sub>O<sub>3</sub> grains. Their volume fraction in the whole sample (~0.1%) was estimated from photoelectron emission micrographs (PEEM) collected at the Co L<sub>3</sub> edge at 781 eV with a relatively large image area (70x70 μm<sup>2</sup>), which contained more than 20 grains.

We observe that these non-epitaxial CFO grains exhibit idiomorphous or hypidiomorphous crystal shapes. Fig. S3 c displays a crystal with almost perfect octahedral shape. Such a shape develops, because crystal growth of CFO starts at lower temperatures than of the surrounding perovskite particles during the sintering process. Hence, CFO grains can “push” the surrounding

material “away”, leading to an unhindered crystal growth and the development of crystal facets according to crystal symmetry, like for crystals growing in a liquid phase. However, we also observe that these grains are permeated by “channels” of the perovskite phase (see Fig. S3). Thus, we conclude that during a later stage of the sintering process, K, Ti and Bi diffuse into the CFO lattice, to form a perovskite structure. Hence, CFO gets effectively “consumed” by the matrix. The formation of core-shell grains can be readily explained in the light of those observations. We assume that in cases where CFO grains are sufficiently small, they act as seeds for growth of perovskite grains, leading to an epitaxial crystallographic relation between the two phases. Subsequently, K, Ti and Bi diffuse into the CFO seed, leading to a grain-boundary migration process, in which the perovskite grain grows at the expense of the CFO seed-grain. The concept of chemically induced grain-boundary migration (CIGM) is well established and has been described in many material systems.[9] However, the diffusion of ions is somewhat limited, and when temperature is reduced after sintering, the grain-boundary migration stops, leading to the observed sharp boundary between core and shell. Thus, we assume that core-shell structures are not thermodynamically stable but are only kinetically stabilized. Furthermore, due to their high chemical potential, corners and edges of the seed grain are consumed faster during grain-boundary migration, leading to the characteristic round edges of cores. However, in cases where CFO grains were already very large at the time of perovskite crystal growth, we assume that seeded growth does not play an important role any more. In those cases, no epitaxial growth occurs and consumption of CFO by the matrix does not occur in a concerted manner from edges towards the center, like in the case of core-shell grains.

A similar core-shell formation mechanism that we suggest above has been described by Koruza et al. for the system of  $(\text{Bi}_{1/2}\text{Na}_{1/2}\text{TiO}_3)_x\text{-(SrTiO}_3)_{1-x}$  (BNT-ST).[10][11] From *in situ* XRD

analysis, the authors concluded that BNT forms at a lower temperature during the calcination process (approx. 600°C) than ST (approx. 800°C), which finally leads to a core-shell structure with BNT-rich cores and ST-rich shells, due to limited diffusion of Sr into BNT grains. For completeness, we want to mention that another slightly different mechanisms of core-shell formation has been described, the so-called reprecipitation mechanism, which involves the formation of a liquid phase that precipitates due to limited solute solubility.[12], [13] The saturation of the melt by the solute leads to a sudden solidification of the liquid phase due to an increase in the melting temperature. However, we rule out this mechanism since it is valid for systems of almost pure BaTiO<sub>3</sub> with only small amounts (few wt. %) of dopants, which is not the case here.

### **Discussion on PFM artifacts and spatial resolution**

We want discuss the possibility of spurious PFM signals measured on CFO cores that could arise not from a piezoelectric response, but from other factors such as differences in contact potential, electric conductivity or electrostatic charges. We have carried out different experiments to understand the origin of signals that we recorded in PFM experiments. As shown in Fig. S3, CFO is present in BFC-BKT ceramics, not only as core-shell particles, but also forms larger single-crystalline particles lacking any crystallographic relation to their surrounding perovskite matrix. These particles exhibit no PFM signal (see left image) since they do not experience epitaxial strain from the perovskite matrix, and thus cannot undergo a non-centrosymmetric lattice distortion like we expect for CFO core particles. However, the non-core-shell particles should still have more or less the same contact potential and electric conductivity as their core-type counterparts, thus spurious PFM signals should also occur here, at least at the interfaces between CFO particle and

matrix. However, the edges are very clear in PFM just like in SEM. Also at interfaces with more conductive materials like metals, we do not observe image artifacts due to gradients in electric conductivity, contact potential or surface charges. We have coated BFC-BKT samples partly with a thin aluminium film (approx. 80 nm). The aluminium film shows no piezo activity in PFM in contrast to BFC-BKT.[14]

Soergel et al. who deposited small copper islands on a PPLN crystal, also observed a 0 PFM signal on top of copper.[15] In general, PFM seems to be also rather robust vs. artifacts, such as electrostatic forces. It was shown by Johann et al. that electrostatically charged surfaces only have an appreciable contribution to PFM signals, for rather soft cantilevers with  $k < 1$  N/m.[16] The cantilevers that we used had a force constant of 11.5 N/m. Furthermore, the relatively high tip load, as used in this contact mode measurement suppresses electrostatic contributions.

Overall, we are confident that the PFM signals that we measured on core-shell type CFO particles are not artifacts arising from differences in contact potential, electric conductivity or surface charges but originate from a direct electromechanical response from the particles themselves.

We want to discuss the plausibility of the amplitude of the PFM signal measured on the CFO core. We carried out many calibration experiments on different days with the same kind of PFM setup (instrument, AFM cantilever model) und settings (AC frequency and voltage) that were used for the measurement in Fig. 3. Here the average PFM signal difference when crossing a  $180^\circ$  domain wall ( $180^\circ$  polarization inversion) was  $0.97 \pm 0.37$  V (uncertainty given by standard deviation).[6] In case of the ferroelectric or non-ergodic region in Fig. 3d, the maximum is approx. 0.3 V. We do not know the out-of-plane polarization component of the FE region. However, the signal intensity of this domain is larger than the average of the statistically distributed polarizations

of other FE region, with the same sign of PFM signal in Fig. 3d. Therefore, we assume that the out-of-plane angle of its polarization vector should be at least  $45^\circ$ . Furthermore, the piezoresponse of the matrix (ergodic region) is approx. 0 since it exhibits relaxor properties and only becomes ferroelectric under sufficiently large electric-fields. Therefore, we estimate the local  $d_{33}$  coefficient to be up to  $0.3 \text{ V}/\sin(45^\circ) = 0.42 \text{ V}$ . This would correspond to a  $180^\circ$  polarization inversion of  $0.84 \text{ V}$  and is thus 13% lower as the average value for PPLN. This means that the local piezoelectric coefficient of the FE regions should be similar to that of  $\text{LiNbO}_3$ , with a moderate  $d_{33}$  coefficient of  $20 \text{ pm/V}$ [7] compared to good piezoelectric materials such as PZT with  $d_{33}$  in the order of  $500\text{-}1000 \text{ pm/V}$ . This is in line with the fact, that the low field piezoelectric coefficient on poled BFC-BKT samples as measured by a conventional Berlincourt meter is only  $16 \text{ pm/V}$ . [1] Therefore, we think it is realistic that the piezoresponse of CFO cores are approx.  $1/3$  of ferroelectric regions.

Due to the small AFM tip radius of below  $100 \text{ nm}$ , the electric field in PFM is concentrated in a very small volume underneath the tip and can reach very high magnitudes in the order of  $108 \text{ V/m}$ . [8] Thus, the particle size only has an influence on PFM-signals for very small particles. The electric field decays quickly to 5% of its maximum value within a distance of approx.  $2 r$  from the tip apex, [9] which corresponds to a depth of  $200 \text{ nm}$  in this case (tip radius  $100 \text{ nm}$ ), thus the piezoresponse is probed very locally. The diameter of the particle is approx.  $500 \text{ nm}$ , which is sufficiently large for an accurate measurement of the particle's piezoresponse. This is in line with the fact, that we see a saturation of the PFM signal over a distance of approx.  $100 \text{ nm}$  around the particle's centre, while the width of the particle borders is also approx.  $100 \text{ nm}$  wide.

## TEM investigation

Fig. S4 a shows a selected area diffraction (SAD) pattern of a BFO-rich phase.  $\frac{1}{2}(000)$  superstructure reflections occur along the  $[\bar{1}\bar{1}0]_c$  zone axis. Note that this notation refers to an orthogonal coordinate system like in the cubic system, which we will use henceforth.  $\frac{1}{2}(000)$  superstructure reflections are presumably due to anti-phase octahedral tilting around the  $[111]_c$  direction ( $a^*a^*a^*$  in glazer notation), which indicates a rhombohedrally distorted perovskite structure like in bulk BFO.[17]. Fig. S4 b shows a dark-field (DF) TEM image of a grain containing a BFO-rich region in the centre, which was recorded using the  $\frac{1}{2}(11\bar{1})$  superstructure reflection as marked by red circle in Fig. S4 a.

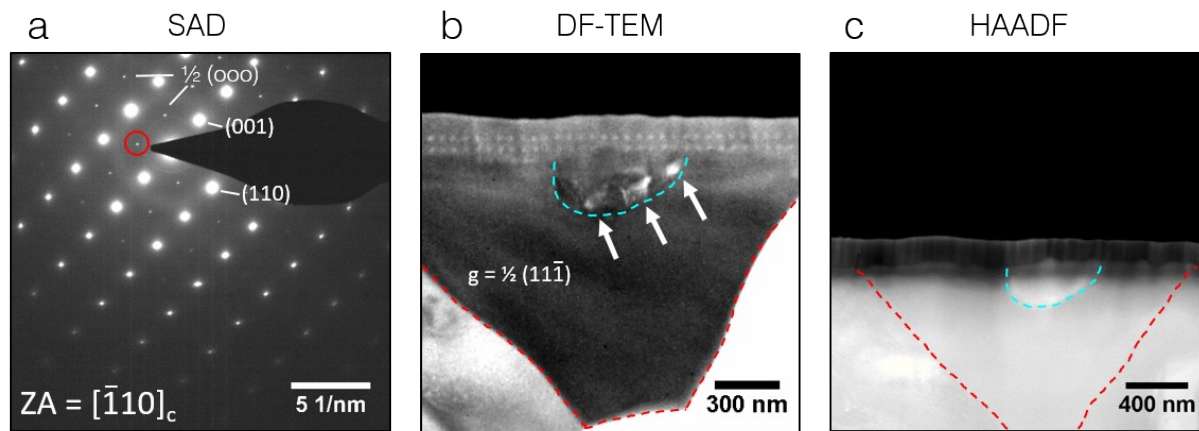


**Figure S4. TEM characterisation of BFC-BKT ceramic by diffraction.** a) Selected area diffraction of BFO-rich region as marked by cyan dashed line in b) and c) along the  $[\bar{1}\bar{1}0]_c$  zone axis, showing  $\frac{1}{2}(000)$  ( $o = \text{odd}$ ) superlattice reflections. b) Dark-field (DF) TEM image recorded using the  $\frac{1}{2}(11\bar{1})$  superstructure reflection as marked by red circle, illustrating that the superstructure is only present in the BFO rich region. c) HAADF-STEM image showing the boundaries of the BFO-rich region.

Note, that in the upper FFT in Fig. 2 h showing the perovskite structure, these superstructure peaks are absent, since they are not visible in every  $\langle 110 \rangle$  zone axis variant.[17] A  $\langle 110 \rangle$  zone axis variant showing the superstructure reflections could not be reached for the core-shell grain depicted in Fig. 2 e.

DF-TEM reveals that the superstructure is only present in the BFO-rich region. The boundaries of the BFO-rich region are visible in HAADF (Fig. S4 c). For clarity, the boundaries of the grain and the BFO rich region inside the grain are marked by dashed lines in HAADF and DF-TEM. The observation of the superstructure in the BFO-rich phase is in line with reports by Ozaki et al., who found the same superstructure reflection in ceramics with composition  $x = 0.6$ ,  $(\text{BiFeO}_3)_x$ - $(\text{Bi}_{1/2}\text{K}_{1/2}\text{TiO}_3)_{1-x}$ [18] since we determined a very similar composition,  $x = 0.66 \pm 0.06$ , for the BFO-rich phase.

In an attempt to further support the assumed polar distortion of CFO cores, we tried to carry out in depth TEM characterization. Since it is difficult to employ selected area diffraction on the small (below 250 nm) CFO cores, we tried to collect further HR-TEM micrographs. We collected HR-TEM micrographs from different crystallographic orientations, which were fast Fourier-transformed to obtain the reciprocal lattice. We did observe distortions from cubic symmetry, but concluded that these were too small to distinguish them confidently from potential image distortions. The microscope that we used (FEI Titan) has an uncertainty of 1% regarding lattice strain, which is almost equal to for example the ferroelectric strain for rhombohedral bulk  $\text{BiFeO}_3$  ( $c/a = 1.01$ ).[1]

## **Dislocations at the core-shell interface**

Fig. S5 shows an HR-TEM micrograph of the core-shell grain boundary where misfit dislocations are marked. Bright patches of contrast appear with a certain periodicity in HR-TEM, which we assign to dislocations. There is one lattice mismatch per 13 to 19 lattices (roughly one dislocation per 5 to 7 nm) in the perovskite phase, which fits well to the mismatch of 6%. The dislocations relax the stress due to the misfit.

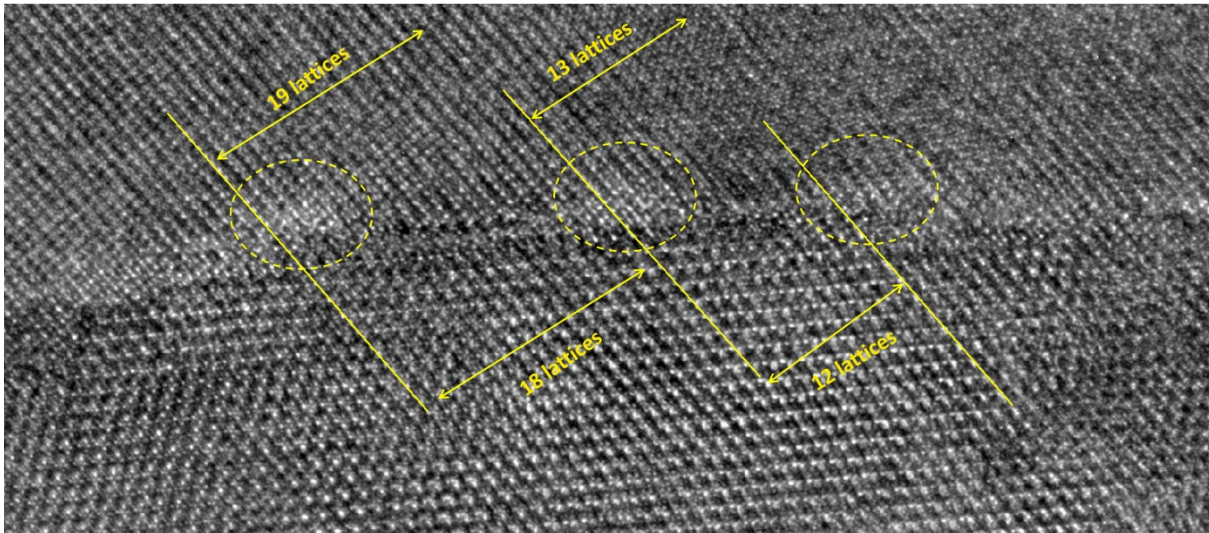


**Figure S5 HR-TEM of core-shell grain boundary.** High-angle annular dark-field (HAADF)-STEM image and corresponding EDX elemental composition maps. Bright patches of contrast are due to misfit dislocations, which appear every 13 to 19 lattices of the perovskite phase.

### **Macroscopic ME measurements**

We carried out in-situ magnetization under electric field measurements using a superconducting quantum interference device (SQUID). Since samples were not textured, we had to magnetize them before the measurement by a large external magnetic field (0.5 T) to measure any net macroscopic coupling coefficient. The sample had a plate-capacitor-like form to be able to apply a uniform electric field across the sample. Furthermore, measurements were made at or close to

the remanent magnetization of the sample so that magnetic moments could relax freely under electric field without being influenced by an external magnetic field. However, the remanent magnetization  $M_R$  is very low compared to the saturation magnetization  $M_S$  ( $M_R/M_S \sim 0.1$ ) meaning that most of the moments are already randomized at or close to zero magnetic field.

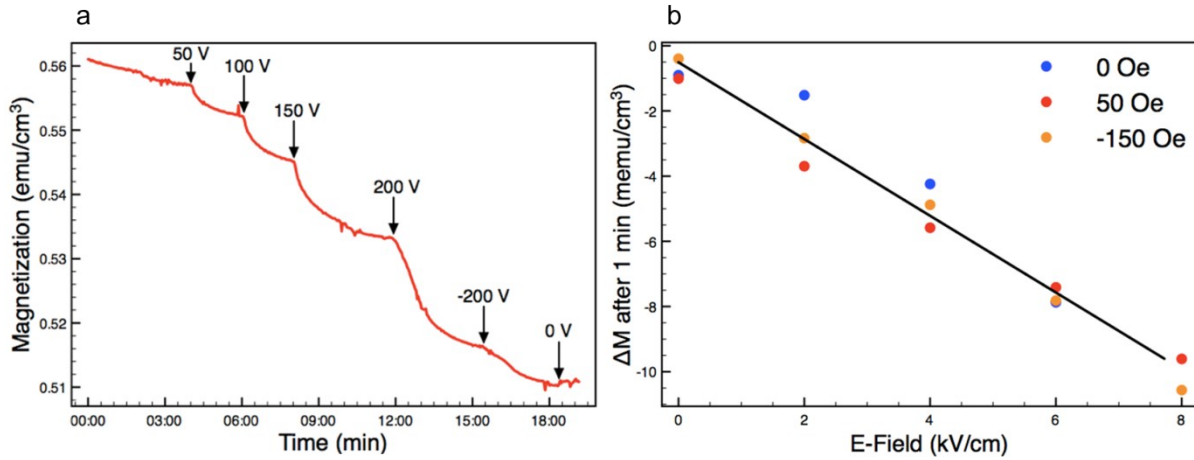


**Figure S6 In-situ magnetization under electric field measurements.** a, Magnetization vs. time measurements at 50 Oe with applied voltages as indicated by labels. b, Change of magnetization after one minute of electric field application vs. electric field at different DC magnetic fields.

Fig. S6 a shows the change of remnant-magnetization over time. Upon application of electric fields, changes in remnant-magnetization are clearly visible. While magnetization relaxes slowly with time without an electric field, relaxation is much faster under applied electric field. After electric field application the relaxation rate slowly approaches the initial relaxation rate. Even for an opposite electric field, the remnant-magnetization still decreases, although the effect is not exactly the same. The fact that inversion of the electric field proves, that the ME effect is not an artifact due to leakage current. If the measured change in magnetic moment was due to a magnetic field induced by a leakage current through the sample, it would also change its sign with a change of the direction of electric field. The change of magnetization (recorded after one minute of electric

field application) as function of electric field in Fig. S6 b, follows a linear trend which is shown in the plot on the right hand side. The effect is similar if no or small magnetic fields are applied during the measurement.

The fact that the magnetization is decreased by applied electric fields can be understood when considering the polycrystalline structure of the sample. Due to the random orientation of microcrystallites, the reorientation of magnetic moments by the electric field is supposedly random as well, which results in a decrease of the net magnetization. In this light, it is also coherent that an inverted electric field has a similar effect.

These measurements suggest a macroscopic coupling coefficient of  $\alpha_{c,eff} = 1.50 \times 10^{-11}$  s/m. This coefficient is much lower than the local coupling coefficient as reported above. However, the coupling coefficient can be understood when considering (i) the low volume concentration of ME core-shell grains and (ii) the fact that the samples were not textured. A net macroscopic coupling coefficient could only be measured, because the sample was magnetized before the measurement by a large external magnetic field which was removed for the ME measurement. Applying the electric field supposedly lead to a relaxation of magnetization due to randomization of magnetic moments carried by the CFO cores. Furthermore, measurements were made at or close to the remanent magnetization of the sample so that magnetic moments could relax freely under electric field without being influenced by an external magnetic field. However, the remanent magnetization  $M_R$  is very low compared to the saturation magnetization  $M_S$  ( $M_R/M_S \sim 0.1$ ) meaning that most of the moments are already randomized at or close to zero magnetic field.

### **$\alpha$ -Fe<sub>2</sub>O<sub>3</sub> core-shell grains**

We note that when comparing Fig. 3 b and f, it becomes clear that not all regions that have a dark contrast in SEM-BSE are also magnetic. This fact is shown more clearly in Fig. S7, which shows correlative SEM, PFM, MFM and elemental mapping by EPMA of a detail of the same sample region as shown in Fig. 3.

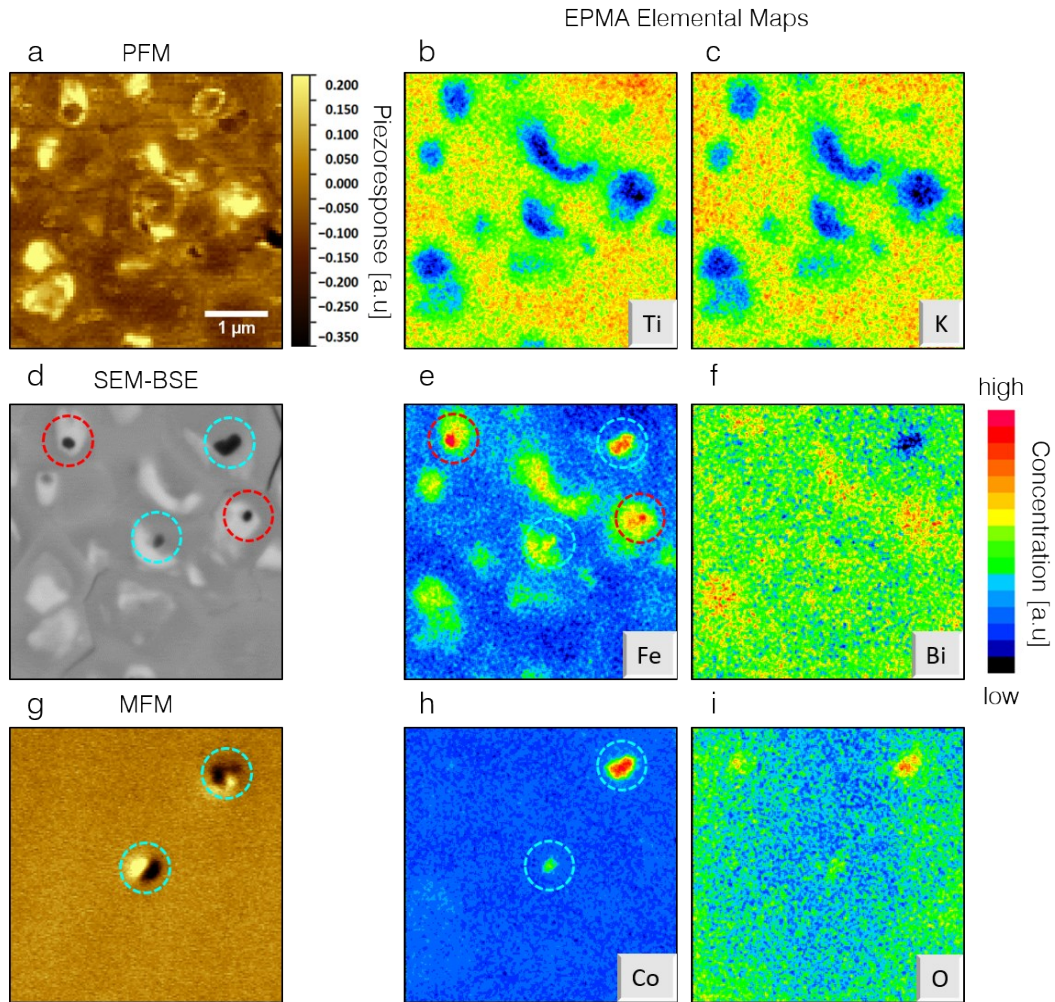


**Figure S7. Correlative scanning probe microscopy and electron microprobe analysis (EPMA).** **a)** VPFM X-Amplitude (mixed signal), **d)** SEM-BSE image, **g)** MFM phase image and **b), c), e), f), h), i)** EPMA elemental maps of the same area on a polished BFC-BKT ceramic. It becomes clear that only CFO cores (marked by cyan dashed circles), which exhibit an increased amount of Co are magnetic. Note that the intensities in elemental maps also depend on the size of

the feature, because the gauge volume is larger than that of the features involved. Other regions which also show a dark contrast in SEM-BSE, presumably consist of  $\alpha$ -Fe<sub>2</sub>O<sub>3</sub> (marked by red dashed circles), since they only contain increased Fe but not Co and are not magnetic.

When comparing Fig. S7 g and h, it is obvious that the two magnetic cores also contain an increased amount of Co and Fe (marked by cyan dashed circles). Note that the intensities in elemental maps also depend on the size of the feature, because the gauge volume of EPMA is larger than that of the features involved. Therefore, the Co intensity for the central CFO core appears to be lower than for the one in the upper right corner. However, this is just an effect of the size of the two cores. On the other hand, other regions exhibiting a dark contrast in SEM-BSE but which are not magnetic (marked by red dashed circles) do not contain an increased amount of Co but more Fe. STEM-EDX analysis revealed that these regions consist of an iron oxide with Fe content of roughly 40%. Since this iron oxide is not magnetic, we conclude that these regions consist of antiferromagnetic  $\alpha$ -Fe<sub>2</sub>O<sub>3</sub>, and not of ferrimagnetic Fe<sub>3</sub>O<sub>4</sub> or  $\gamma$ -Fe<sub>2</sub>O<sub>3</sub>. By using SEM-EDX and MFM, we could test large areas of the sample for both elemental composition and magnetic properties to be able to say that the correlative microscopy data as presented in Fig. S7 are representative of the whole sample.

This is in line with the fact, that  $\alpha$ -Fe<sub>2</sub>O<sub>3</sub> was used as source of Fe in the synthesis of the ceramic.  $\alpha$ -Fe<sub>2</sub>O<sub>3</sub> seems to also form core-shell structures with the perovskite matrix, which is reasonable since its corundum structure is closely related to the perovskite structure. However, CFO is encountered more frequently in the material.

It is difficult to gauge the amount of epitaxial  $\alpha$ -Fe<sub>2</sub>O<sub>3</sub> and CFO, since they cannot be distinguished just by SEM-BSE contrast but require an EDX analysis. The composition of the dark regions

exhibiting a core-shell type structure was determined in 19 cases by STEM-EDX. From these cases, we estimate that the volume ratio between CFO and  $\alpha$ -Fe<sub>2</sub>O<sub>3</sub> core-grains is roughly 9:1. Furthermore, we estimate the total content of CFO in the whole sample was estimated to be ~3 vol% from magnetometry measurements by taking into account a magnetization  $M_S$  of 14.1 emu/cm<sup>3</sup> due to CFO secondary phases in BFC-BKT ceramics[19] and an  $M_S$  of 455 emu/cm<sup>3</sup> for bulk CFO.[20] We regard the magnetization as the most accurate measure. However, we need to mention that the saturation magnetization could be also significantly lower from sample batch to batch (the example as given above had a rather high value of  $M_S$  as compared to other samples) by a factor of ~3, which indicates that the amount of CFO secondary phase could change from batch to batch. So one might expect the total content of CFO to lie between 1-3%. This is also in qualitative agreement with the intensity of minor peaks due to CFO in X-ray and neutron diffraction, although attempts to quantify the CFO content by Rietveld refinements were unsuccessful. From an SEM-BSE image (area 40x31.7  $\mu\text{m}^2$ ) containing more than 100 dark regions exhibiting a core-shell type structure, we estimated their volume fraction (using an image processing software). The composition of large grains (> 1  $\mu\text{m}$ ), which do not exhibit a core-shell type structure, can be measured much easier by SEM-EDX and we found almost exclusively CFO and very few  $\alpha$ -Fe<sub>2</sub>O<sub>3</sub> grains. Their area fraction was estimated from larger SEM-BSE images (200 x 150  $\mu\text{m}$ ) which contained approx. 20 grains, which leads to a volume fraction between core-shell CFO plus  $\alpha$ -Fe<sub>2</sub>O<sub>3</sub> and large CFO grains of 0.1-0.33. The volume of large grains was further confirmed by photoelectron emission micrographs collected at the Co L<sub>3</sub> edge at 781 eV of a relatively large sample area (70x70  $\mu\text{m}^2$ ), where CFO particles were well visible due to the increased intensity of CFO particles at this photon energy.

## References

- [1] C.-S. Hsu, N.-T. Suen, Y.-Y. Hsu, H.-Y. Lin, C.-W. Tung, Y.-F. Liao, T.-S. Chan, H.-S. Sheu, S.-Y. Chen, and H. M. Chen, “Valence- and element-dependent water oxidation behaviors: in situ X-ray diffraction, absorption and electrochemical impedance spectroscopies,” *Phys. Chem. Chem. Phys.*, vol. 19, no. 13, pp. 8681–8693, Mar. 2017.
- [2] Z. Y. Wu, S. Gota, F. Jollet, M. Pollak, M. Gautier-Soyer, and C. R. Natoli, “Characterization of iron oxides by x-ray absorption at the oxygen K edge using a full multiple-scattering approach,” *Phys. Rev. B*, vol. 55, no. 4, pp. 2570–2577, Jan. 1997.
- [3] P. S. V Mocherla, S. Gautam, K. H. Chae, M. S. R. Rao, and C. Sudakar, “Wide-range tunable bandgap in  $\text{Bi}_{1-x}\text{Ca}_x\text{Fe}_{1-y}\text{Ti}_y\text{O}_{3-\delta}$  nanoparticles via oxygen vacancy induced structural modulations at room temperature,” *Mater. Res. Express*, vol. 2, no. 9, p. 095012, Sep. 2015.
- [4] J. Suntivich, W. T. Hong, Y.-L. Lee, J. M. Rondinelli, W. Yang, J. B. Goodenough, B. Dabrowski, J. W. Freeland, and Y. Shao-Horn, “Estimating Hybridization of Transition Metal and Oxygen States in Perovskites from O K -edge X-ray Absorption Spectroscopy,” *J. Phys. Chem. C*, vol. 118, no. 4, pp. 1856–1863, Jan. 2014.
- [5] C. Pinta, D. Fuchs, M. Merz, M. Wissinger, E. Arac, H. v. Löhneysen, A. Samartsev, P. Nagel, and S. Schuppler, “Suppression of spin-state transition in epitaxially strained  $\text{LaCoO}_3$ ,” *Phys. Rev. B*, vol. 78, no. 17, p. 174402, Nov. 2008.
- [6] C. T. Chen, F. Sette, Y. Ma, M. S. Hybertsen, E. B. Stechel, W. M. C. Foulkes, M. Schuler, S.-W. Cheong, A. S. Cooper, L. W. Rupp, B. Batlogg, Y. L. Soo, Z. H. Ming, A. Krol, and

- Y. H. Kao, "Electronic states in  $\text{La}_{2-x}\text{Sr}_x\text{CuO}_{4+\delta}$  probed by soft-x-ray absorption," *Phys. Rev. Lett.*, vol. 66, no. 1, pp. 104–107, Jan. 1991.
- [7] D. K. Bora, A. Braun, S. Erat, A. K. Ariffin, R. Löhnert, K. Sivula, J. Töpfer, M. Grätzel, R. Manzke, T. Graule, and E. C. Constable, "Evolution of an Oxygen Near-Edge X-ray Absorption Fine Structure Transition in the Upper Hubbard Band in  $\alpha\text{-Fe}_2\text{O}_3$  upon Electrochemical Oxidation," *J. Phys. Chem. C*, vol. 115, no. 13, pp. 5619–5625, Apr. 2011.
- [8] M. Merz, N. Nücker, S. Schuppler, D. Arena, J. Dvorak, Y. U. Idzerda, S. N. Ustinovich, A. G. Soldatov, S. V. Shiryaev, and S. N. Barilo, "X-ray absorption of  $\text{Ba}_{1-x}\text{K}_x\text{BiO}_3$  and  $\text{BaPb}_{1-y}\text{Bi}_y\text{O}_3$ : Competition between bipolaronic and charge-density wave states," *Europhys. Lett.*, vol. 72, no. 2, pp. 275–281, Oct. 2005.
- [9] D. Y. Yoon, "Theories and observations of chemically induced interface migration," *Int. Mater. Rev.*, vol. 40, no. 4, pp. 149–179, Jan. 1995.
- [10] J. Koruza, V. Rojas, L. Molina-Luna, U. Kunz, M. Dürrschnabel, H.-J. Kleebe, and M. Acosta, "Formation of the core-shell microstructure in lead-free  $\text{Bi}_{1/2}\text{Na}_{1/2}\text{TiO}_3\text{-SrTiO}_3$  piezoceramics and its influence on the electromechanical properties," *J. Eur. Ceram. Soc.*, vol. 36, no. 4, pp. 1009–1016, Mar. 2016.
- [11] T. Frömling, S. Steiner, A. Ayrikyan, D. Bremecker, M. Dürrschnabel, L. Molina-Luna, H.-J. Kleebe, H. Hutter, K. G. Webber, and M. Acosta, "Designing properties of  $(\text{Na}_{1/2}\text{Bi}_x)\text{TiO}_3$ -based materials through A-site non-stoichiometry," *J. Mater. Chem. C*, vol. 6, no. 4, pp. 738–744, Jan. 2018.
- [12] D. Hennings and G. Rosenstein, "Temperature-Stable Dielectrics Based on Chemically

- Inhomogeneous BaTiO<sub>3</sub>,” *J. Am. Ceram. Soc.*, vol. 67, no. 4, pp. 249–254, Oct. 1987.
- [13] C. A. Randall, S. F. Wang, D. Laubscher, J. P. Dougherty, and W. Huebner, “Structure property relationships in core-shell BaTiO<sub>3</sub>–LiF ceramics,” *J. Mater. Res.*, vol. 8, no. 4, pp. 871–879, 1993.
- [14] L. F. Henrichs, L. I. Chen, and A. J. Bell, “Simple technique for high-throughput marking of distinguishable micro-areas for microscopy,” *J. Microsc.*, vol. 262, no. 1, pp. 28–32, Apr. 2016.
- [15] E. Soergel, “Piezoresponse force microscopy (PFM),” *J. Phys. D Appl. Phys.*, vol. 44, no. 46, p. 464003, 2011.
- [16] F. Johann, Á. Hoffmann, and E. Soergel, “Impact of electrostatic forces in contact-mode scanning force microscopy,” *Phys. Rev. B*, vol. 81, no. 9, p. 94109, 2010.
- [17] D. I. Woodward, I. M. Reaney, IUCr, C. D. E., S. N., C. D. E., and S. G., “Electron diffraction of tilted perovskites,” *Acta Crystallogr. Sect. B Struct. Sci.*, vol. 61, no. 4, pp. 387–399, Aug. 2005.
- [18] T. Ozaki, H. Matsuo, Y. Noguchi, M. Miyayama, and S. Mori, “Microstructures Related to Ferroelectric Properties in (Bi<sub>0.5</sub>K<sub>0.5</sub>)TiO<sub>3</sub>–BiFeO<sub>3</sub>,” *Jpn. J. Appl. Phys.*, vol. 49, no. 9S, p. 09MC05, 2010.
- [19] L. F. Henrichs, O. Cespedes, J. Bennett, J. Landers, S. Salamon, C. Heuser, T. Hansen, T. Helbig, O. Gutfleisch, D. C. Lupascu, H. Wende, W. Kleemann, and A. J. Bell, “Multiferroic Clusters: A New Perspective for Relaxor-Type Room-Temperature Multiferroics,” *Adv. Funct. Mater.*, vol. 26, no. 13, pp. 2111–2121, Feb. 2016.

- [20] F. Eskandari, S. B. Porter, M. Venkatesan, P. Kameli, K. Rode, and J. M. D. Coey, “Magnetization and anisotropy of cobalt ferrite thin films,” *Phys. Rev. Mater.*, vol. 1, no. 7, p. 074413, Dec. 2017.